

Article

A Fault Detection Method Based on CNN and Symmetrized Dot Pattern for PV Modules

Meng-Hui Wang , Zong-Han Lin and Shiue-Der Lu * 

Department of Electrical Engineering, National Chin-Yi University of Technology, Taichung 411, Taiwan
* Correspondence: sdl@ncut.edu.tw; Tel.: +886-4-23924505 (ext. 7260)

Abstract: The photovoltaic (PV) module is a key technological advancement in renewable energy. When the PV modules fail, the overall generating efficiency will decrease, and the power system's operation will be influenced. Hence, detecting the fault type when the PV modules are failing becomes important. This study proposed a hybrid algorithm by combining the symmetrized dot pattern (SDP) with a convolutional neural network (CNN) for PV module fault recognition. Three common faults are discussed, including poor welding, breakage, and bypass diode failure. Moreover, a fault-free module was added to the experiment for comparison. First, a high-frequency square signal was imported into the PV module, and the original signal was captured by the NI PXI-5105 high-speed data acquisition (DAQ) card for the hardware architecture. Afterward, the signal was imported into the SDP for calculation to create a snowflake image as the image feature for fault diagnosis. Finally, the PV module fault recognition was performed using CNN. There were 3200 test data records in this study, and 800 data records (200 data records of each fault) were used as test samples. The test results show that the recognition accuracy was as high as 99.88%. It is better than the traditional ENN algorithm, having an accuracy of 91.75%. Therefore, while capturing the fault signals effectively and displaying them in images, the proposed method accurately recognizes the PV modules' fault types.

Keywords: photovoltaic module; symmetrized dot pattern; convolutional neural network



Citation: Wang, M.-H.; Lin, Z.-H.; Lu, S.-D. A Fault Detection Method Based on CNN and Symmetrized Dot Pattern for PV Modules. *Energies* **2022**, *15*, 6449. <https://doi.org/10.3390/en15176449>

Academic Editor: Alon Kuperman

Received: 17 August 2022

Accepted: 30 August 2022

Published: 3 September 2022

Publisher's Note: MDPI stays neutral with regard to jurisdictional claims in published maps and institutional affiliations.



Copyright: © 2022 by the authors. Licensee MDPI, Basel, Switzerland. This article is an open access article distributed under the terms and conditions of the Creative Commons Attribution (CC BY) license (<https://creativecommons.org/licenses/by/4.0/>).

1. Introduction

The global energy demand has increased in recent years. Renewable energy sources (RESs) have been the future trend of power generation [1–3]. PV is one of the key technological advancements. It has been accepted and used worldwide [4]. The PV panel may be damaged during manufacturing, construction, transportation, and improper installation. These damages can lead to faults [5]. The common fault types in many PV accident reports include poor welding [6], breakage [7], bypass diode failure [8], line-to-ground (L-G) and line-to-line (L-L) faults [9,10], partial shading and short-circuit of bypass diodes faults [11], and arc faults [12]. Many experts propose using machine learning and deep learning for PV module fault diagnosis [13–20]. Ref. [13] proposed a PV bypass diode detection algorithm and used three series-connected PV modules and nine bypass diodes for experimental evaluation. The accuracy varied with time, but in mismatched conditions, e.g., shadow, hot spot, welding, or stratification, the values of I_{sc} and V_{mpp} decreased. Ref. [14] introduced the support vector machine (SVM) classifier to PV module defective parts including parallel cracks, series cracks, bypass diode failure, and defective-free from electroluminescence (EL) images. The results showed that the method had an accuracy of 97.5%. However, the method only focused on the bypass diode and the PV module with parallel and series cracks faults. Additionally, the EL equipment needed to be used first to obtain the images for the feature extraction procedures. Ref. [15] proposed a random forest algorithm for PV module fault diagnosis, including five fault types. These five fault types include open circuit, short circuit, hot spot, aging, and partial shading. The experimental results showed

that the accuracy ranged from 60% to 80%. The method is effective in PV module fault diagnosis. Ref. [16] proposed a method based on ENN and the chaos synchronization detection method (CSDM) and constructed three common fault types, including PV component damage, PV component aging, and PV component bypass diode fault. The recognition accuracy was as high as 87.5%. The method is characterized by compressing Big Data and extracting effective feature values. The trained ENN is used for identifying the fault type. Ref. [17] proposed a hybrid algorithm of CSDM and CNN and used four common PV component states, including normal PV component, component damage, component contact defect, and module bypass diode fault for experimental evaluation. The recognition accuracy was as high as 99.5%. The method uses CSDM to reduce a large number of original measured data. Subtle changes in output signals are displayed in the image effectively so the CNN can accurately identify the PV component fault state. Ref. [18] proposed a fully convolutional network (FCN) method, especially for detecting bird's drops on the surface of PV modules. A multi-copter for autonomous aerial monitoring of PV plants also was used to obtain the images of the PV modules. The results showed that the proposed method can detect pixels covered by bird's drops with an average accuracy of 93%. However, the method only focused on the visible failures of PV modules. The multi-copter also needed to be utilized for screening the feature images of PV plants. It really depends on the professional operation to control the multi-copter for receiving suitable images. Ref. [19] introduced the principal component analysis (PCA) algorithm with a support vector machine (SVM) based on an I-V curve of solar cells for short circuit and shading faults. The method identified only two types of PV fault and needed information on the I-V curve of PV. Ref. [20] conducted an artificial neural network to detect the DC side of PV faults with an accuracy of 83%. The fault types included partial shading, L-L, open circuit, degradation, bypass diode, and bridge faults. However, the method is only used for a simulation model rather than the real PV systems. The above-mentioned references for different methods, PV fault types, and performances are listed in Table 1.

Table 1. Literature review of fault detection method and accuracy rate for PV system.

| Methods | Fault Types | Cracks | Bypass Diode Failure | Aging | Open Circuit | Short Circuit | Hot Spot | Partial Shading | Accuracy Rate (%) |
|--------------------|-------------|--------|----------------------|-------|--------------|---------------|----------|-----------------|-------------------|
| SVM [14] | | ✓ | ✓ | | | | | | 95 |
| Random forest [15] | | | | ✓ | ✓ | ✓ | ✓ | ✓ | 60~80 |
| CSDM + ENN [16] | | ✓ | ✓ | ✓ | | | | | 87.5 |
| CSDM + CNN [17] | | ✓ | ✓ | ✓ | | | | | 99.5 |
| FCN [18] | | ✓ | | | | | | | 93 |
| SVM [19] | | | | | ✓ | ✓ | | ✓ | 90 |
| ANN [20] | | | ✓ | | ✓ | | | ✓ | 95 |

While most studies focus on the PV modules and bypass diode faults using neural network-related methods, there has been limited literature proposed using CNN with SDP (the feature extraction method). Therefore, a hybrid algorithm proposed in this study combines SDP and CNN for PV module fault diagnosis. The PV module fault models were constructed based on the normal state (Type 1) and three common fault types, including poor welding of a PV module (Type 2), a PV module breakage (Type 3), and a PV module diode bypass failure (Type 4). This study built an intelligent deep learning method detection system for PV modules based on CNN combined with SDP for identifying PV faults and used 800 samples for the experiment. First, the high-frequency signal was imported into the PV module to capture the original output signal, which led to the SDP obtaining a snowflake image as a feature map [21,22]. Then, the fault type was identified using CNN [23]. The proposed SDP is highly sensitive to input signals. As a result, if the input signal changes slightly, the image output result will show the differences, which is favorable for extracting meaningful feature values from the fault signals.

2. Architecture and Design of the Research System

Two main parts, including the overall system detection process architecture, a fault testing platform, and the PV module fault-type construction, are discussed in this chapter. First, the overall system detection process contains waveform generators, DAQ equipment, various PV modules, and the proposed method. Second, the fault-testing platform and how to build up the failure of PV modules are detailed discussion as follows.

2.1. The Overall System Detection Process Architecture

The detection system developed in this study can analyze signals in different PV fault conditions by combining SDP with CNN for diagnosis. Figure 1 shows the overall system detection process architecture. A high-frequency voltage was imported into the different fault models, and the original signal was captured by a PXI high-speed DAQ card from the output signal waveform as the data analysis source of fault diagnosis. SDP then converted the failure data into a snowflake image, and the fault type was identified using CNN.

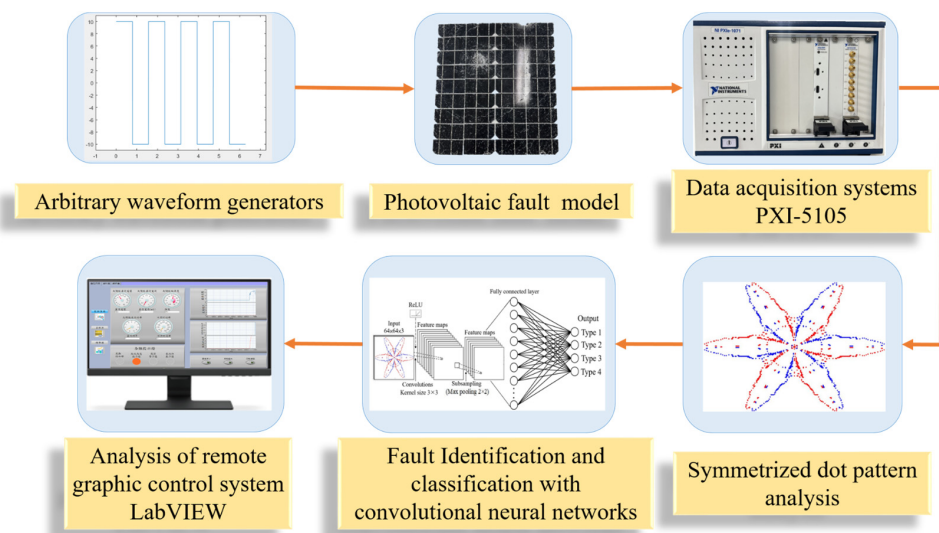


Figure 1. The overall system detection process architecture.

2.2. A Fault-Testing Platform and PV Module Fault-Type Construction

The PV module fault detection testing platform built in this study is shown in Figure 2. The waveform generator (Agilent 33220A) was used as a signal source. A 250 kHz square wave was imported via the anode and cathode of the PV module. The test data were captured by PXI-5105 and fed into the algorithm for fault recognition.

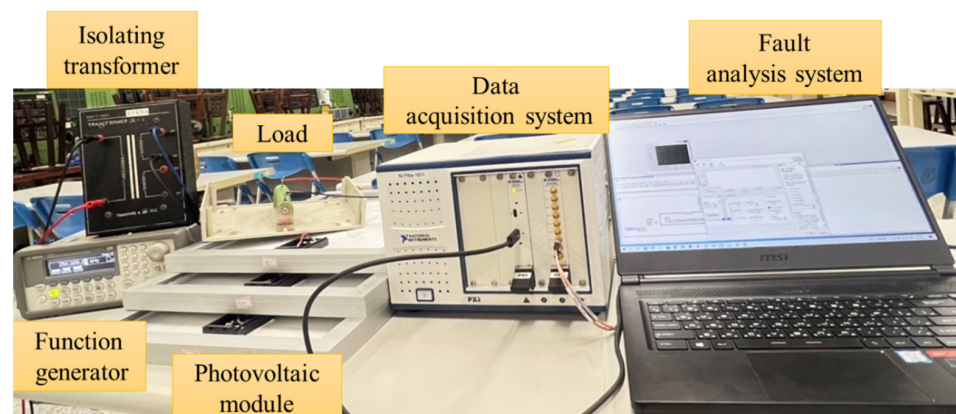


Figure 2. PV module fault detection testing platform.

Four common PV module fault-state models were built in this study, as shown in Table 2, including normal module (Type 1), poor welding (Type 2), module breakage (Type 3), and diode bypass failure (Type 4). The different signal results of the PV modules measured in different fault conditions were discussed. Then, the image feature map was generated by SDP and identified by CNN.

Table 2. The fault-state models of a PV module.

| PV module types |
|---------------------------------------|
| Normal PV module (Type 1) |
| Poor connection of PV module (Type 2) |
| PV module breakage (Type 3) |
| Bypass diode failure (Type 4) |

2.2.1. Normal PV Module (Type 1)

This study used a 20 W monocrystalline silicon PV module, as shown in Figure 3, in the standard test condition (the irradiance level at 1000 W/m^2 , the mass of atmosphere at air mass 1.5, and the temperature at $25 \text{ }^\circ\text{C}$). The rated voltage, rated current, open-circuit voltage, and short-circuit current of the PV module were 18.2 V, 1.10 A, 22.4 V, and 1.19 A, respectively.

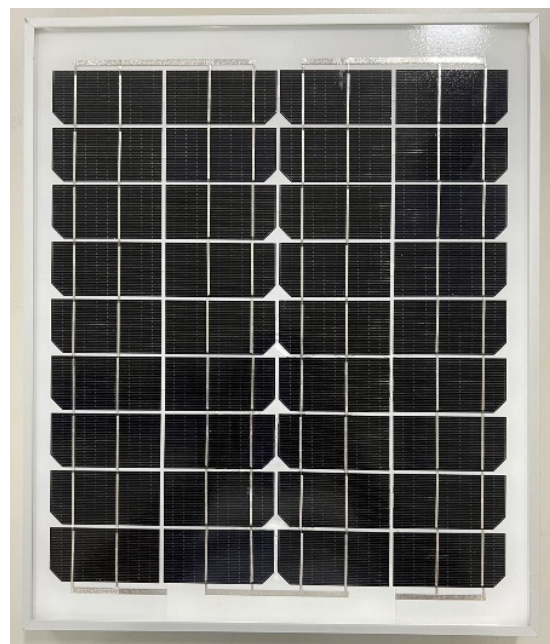


Figure 3. Normal PV module.

2.2.2. Poor Connection on a PV Module (Type 2)

As the electrical equipment runs for a long time or the ambient temperature changes, the type of material or the installed structure may loosen the screws or pressure connection terminals of a power circuit, leading to safety problems. According to [24], the primary cause of electrical equipment aging or failure is the loosening of welding adhesive or grid-line interface breakage. This study added an electronic load to the PV module, and additional loads of 2Ω and 10Ω were applied to study the poor connection. The resistance was divided into ten equal parts and was adjusted from 1Ω to 10Ω to construct the aging fault type, as shown in Figure 4.

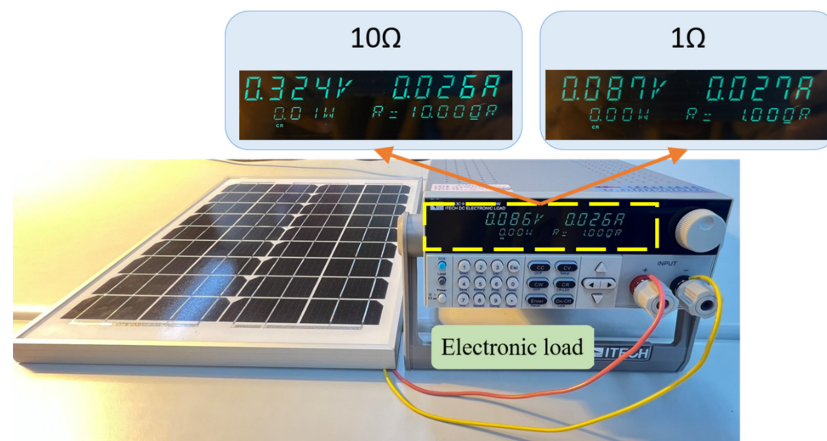


Figure 4. A poor connection of a PV module.

2.2.3. PV Module Breakage (Type 3)

This study used severe and light damage models to study the broken module, as shown in Figures 5 and 6. According to [25], the structure of a module varies with environmental factors. The faults were divided into safety and performance faults. The PV module breakage was a safety fault. This study used an external force for impact damage to the full set of PV modules to simulate the PV module damage induced by human stepping and foreign object damage during construction. The damage extended from the knocking point to the periphery to induce the loss of normal function in other silicon wafers.

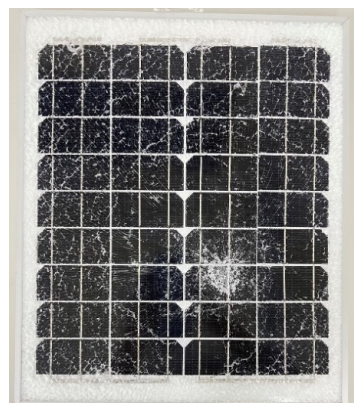


Figure 5. Severe breakage of the PV module.

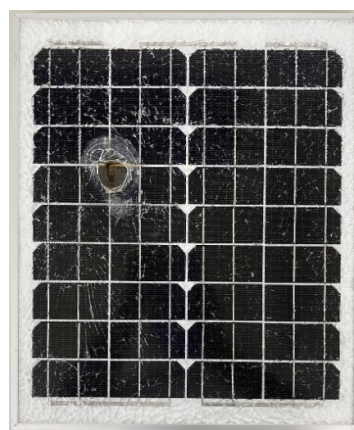


Figure 6. Mild breakage of the PV module.

2.2.4. Bypass Diode Failure (Type 4)

The PV module is inevitably influenced by external factors in the course of PV conversion, and the electricity generation is reduced [26]. The damaged battery or the shaded module area begins to heat up, and the bypass diode exerts a significant effect. The current can pass by the shaded PV module to reduce the hot spot effect. The bypass diode of the normal PV module was shorted in this study. A conductor was welded to short the bypass diode, and the anode of the diode was cut, as shown in Figures 7 and 8.



Figure 7. Diode short circuit.



Figure 8. Diode open circuit.

3. Research Methods

This study aims at PV module fault diagnosis. First, a 250 kHz and 20 Vp-p high-frequency square-wave signal was imported. The data were captured by PXI 5105 to read the measured signal of the PV module fault type. SDP converted the time domain waveform signals into a polar-coordinate symmetrized snowflake image, and the fault type was identified by CNN. The analysis process is shown in Figure 9. The SDP and CNN are described below.

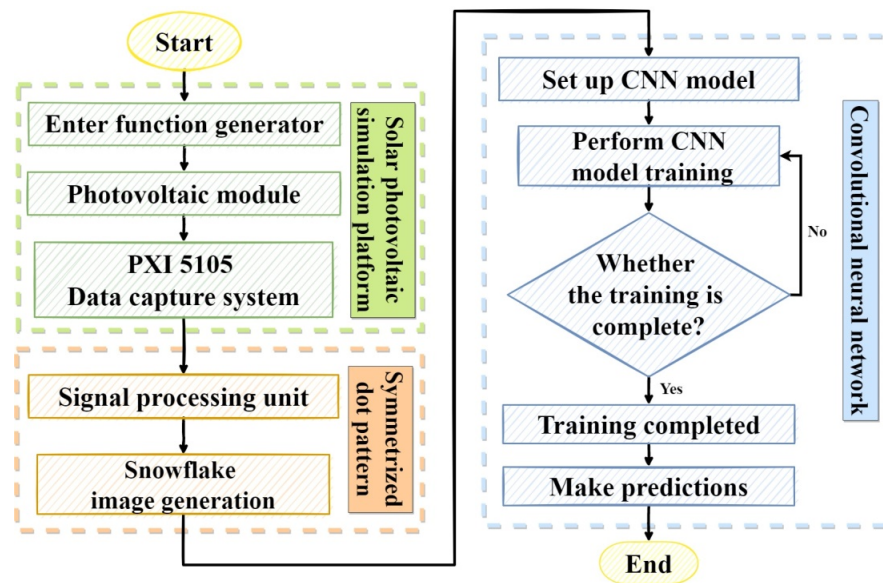


Figure 9. Fault recognition analysis process.

3.1. SDP

The SDP converts the original signal of PV into a snowflake image as the feature map. Different snowflake images are generated as the PV module fault signal changes. Figure 10 shows the snowflake image of a normal PV module.

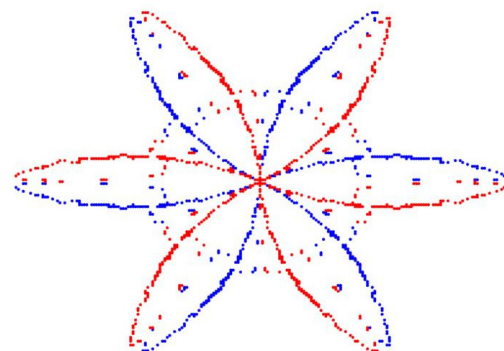


Figure 10. Snowflake image of the normal PV module.

The SDP uses a data acquisition system to convert the data of time-domain square-wave signals into a polar-coordinate feature image. Figure 11 shows the principle of the method, where (i) is the radius of the polar coordinates in the snowflake image; $\theta_{cw}(i)$ is the clockwise rotation angle of the x-axis; $\theta_{ccw}(i)$ is the counterclockwise rotation angle of the x-axis. In the square-wave data sampling of the PV module state signals, the signal sampling point x_i is the i^{th} sampling point of signal x , the signal sampling point $x_{i+\tau}$ is the sampling point at No. $i + \tau$ time of signal x . These are substituted in Equations (1)–(3). The point of the converted polar coordinate space is $O(r(i), \theta_{cw}(i), \theta_{ccw}(i))$. The PV module state signal can be generated by changing the initial rotation angle to form the symmetric image of point coordinates.

$$r(i) = \frac{x_i - x_{min}}{x_{max} - x_{min}} \tag{1}$$

$$\theta_{cw}(i) = \theta - \frac{x_{i+\tau} - x_{min}}{x_{max} - x_{min}} S \tag{2}$$

$$\theta_{ccw}(i) = \theta + \frac{x_{i+\tau} - x_{min}}{x_{max} - x_{min}} S \tag{3}$$

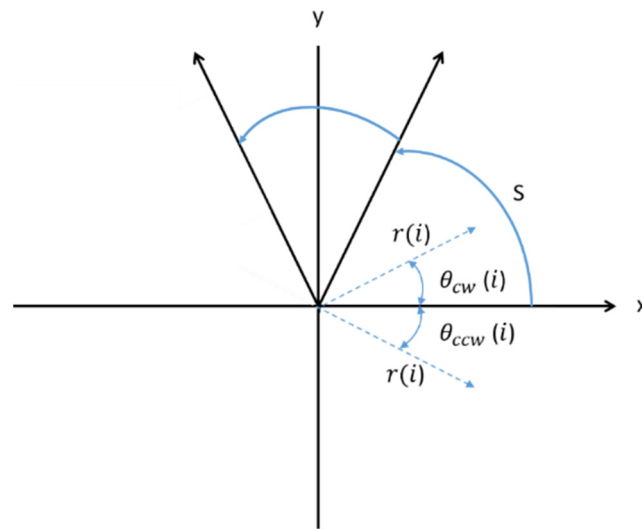


Figure 11. Snowflake image calculation principle.

The x_{max} in Equations (1)–(3) is the maximum value of the original signal; x_{min} is the minimum value of the original signal; τ is the signal interval time parameter ($1 \leq \tau \leq 10$); θ is the initial deflection angle of the x-axis; S is the amplification coefficient of the rotation angle ($S \leq \theta$). The test result shows that the feature map parameters suitable for PV module fault recognition analysis were $\theta = 60^\circ$, $\tau = 3$, and $S = 3$.

3.2. Convolutional Neural Networks (CNN)

By using SDP in this study, the time-domain waveform was converted into a polar image so that the feature image could be led in the CNN for PV module fault model recognition. The CNN converts and extracts useful feature maps. It is one of the most used methods and is mostly used for image identification functions, e.g., mechanical vibration fault diagnosis monitoring [27] and PV array fault classification [28,29].

The CNN architecture is shown in Figure 12. CNN is a neural network architecture that uses the convolution layer and the pooling layer to extract features from the input image. The feature picture can be extracted by multiple cyclical steps of convolution and pooling layers. The feature map is handed to the fully connected layer for classification, and the output result is obtained at last.

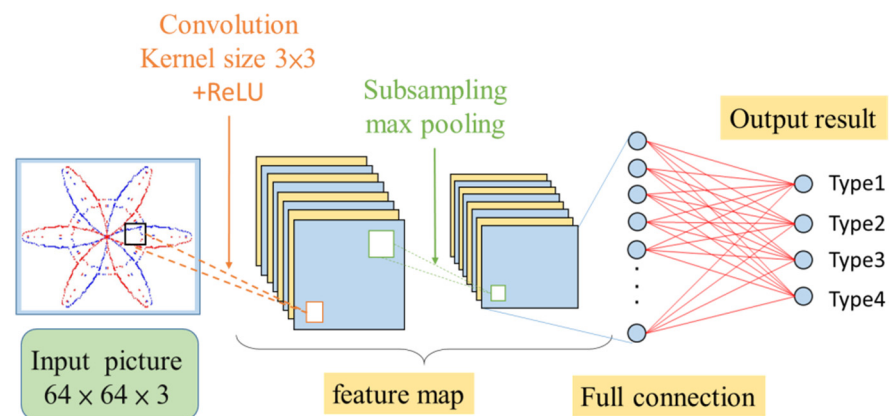


Figure 12. A CNN architecture.

3.2.1. Function of Convolution Layer

The convolution layer acts as the image feature extractor in the CNN. This layer uses a convolution kernel or a filter of different sizes for the convolution layer operation. The image feature value access or feature optimization is performed by spatial filtering factors.

Specifically, a convolution kernel of 3×3 is usually taken as an example and stacked on a 6×6 image. Two corresponding cells are multiplied, and the numerical results of 9 products are added to obtain new image values. The unit of each move is one stride, and the whole 6×6 image is scanned to obtain the feature map, expressed as Equation (4). The convolution operation mode is shown in Figure 13 [30].

$$x_j^l = f \left(\sum_{i \in M_j} x_j^{l-1} \cdot W_{ij}^l + b_j^l \right) \tag{4}$$

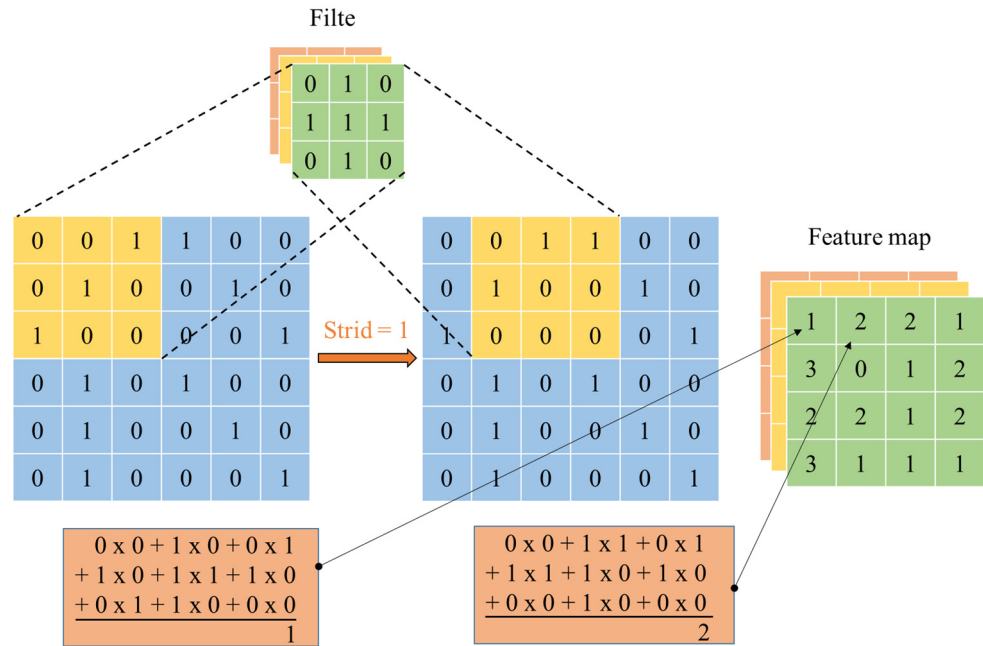


Figure 13. The operational method of the convolution layer.

In the mathematical expression, x_j^l is No. j element of layer l; M_j is No. j convolution region of $l - 1$ layer feature image; x_j^{l-1} is the element therein; W_{ij}^l is the weighting matrix corresponding to the convolution kernel; b_j^l is the deviation; $f(\cdot)$ is in the activation function. The ReLU activation function was used in this study and expressed in Equations (5) and (6).

$$f(x) = \max(0, x) \tag{5}$$

$$f(x) = \begin{cases} x, & \text{if } x \geq 0 \\ 0, & \text{if } x \leq 0 \end{cases} \tag{6}$$

3.2.2. Function of the Pooling Layer

The pooling layer also has a filter to scan the whole image. The pooling layer is divided into two parts: max pooling and average pooling. This process aims to further compress the image data, with the most excellent characteristic of the feature map being reflected. The 4×4 image feature, obtained after the convolution layer operation, is cut up into 2×2 parts. The maximum value and the average value of the segmented part are extracted and placed in the 2×2 matrix of max pooling and average pooling. The data after pooling maintain the essential features of the original image. Figure 14 shows the operation mode of the pooling layer.

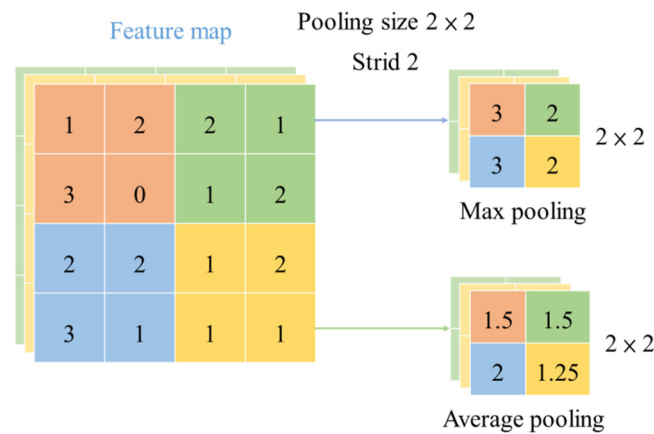


Figure 14. The operation mode of the pooling layer.

As shown in Equation (7), $down(\cdot)$ is the downsampling function; it often has max pooling, average pooling, and general pooling. This study took max pooling and average pooling as the examples. The featured image exported to the convolution layer was pooled in each $n \times n$ nonoverlapping area. A maximum value in each area was selected, and the size of the final output image was reduced n times.

$$x_j^l = (down(x_j^{l-1})w_j^l + b_j^l) \tag{7}$$

3.2.3. Function of Fully Connected Layer

The fully connected layer covers the most fundamental neural network, composed of the flatten layer, hidden layer, and output layer. It convolves and pools the feature map derived from the original image through a series of processing. As the obtained feature map is a 2D image, the flatten layer is required to convert 2D into a 1D array. Finally, the image prediction and classification results are flattened. Figure 15 shows the operation flow of a fully connected layer.

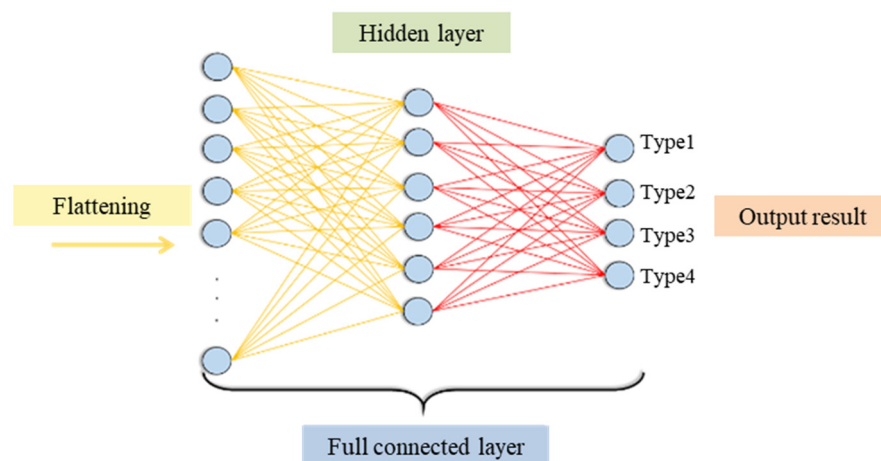


Figure 15. Computing architecture of the fully connected layer.

As shown in Equation (8), x is the input of a fully connected layer; $h(\cdot)$ is the output of a fully connected layer; w is the weight; b is the additive deviation; $f(\cdot)$ is the activation function.

$$h(x) = f(wx + b) \tag{8}$$

4. Experimental Results

This study had four types of PV modules, including a normal module, a poor connection on the module, module breakage, and bypass diode failure. Four kinds of square-wave output signals measured by this system are shown in Figures 16–19. First, a high-frequency 250 kHz signal was imported with the input voltage of a 20 V_{pp} high-frequency square-wave signal. The data sampling time was 40 μ s, totaling ten periods. The failure data of 3200 points were sampled. As four state models were built, 200 samples of data were extracted from each model, totaling 800 samples for the experiment.

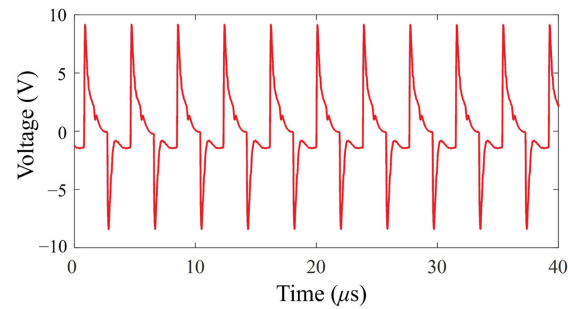


Figure 16. Normal signals of a PV module.

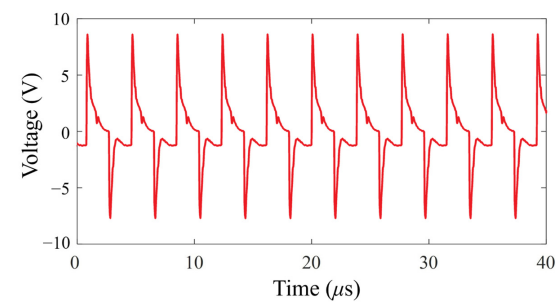


Figure 17. Poor connection signals of a PV module.

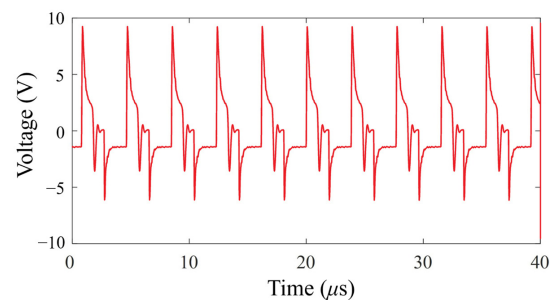


Figure 18. PV module breakage signals.

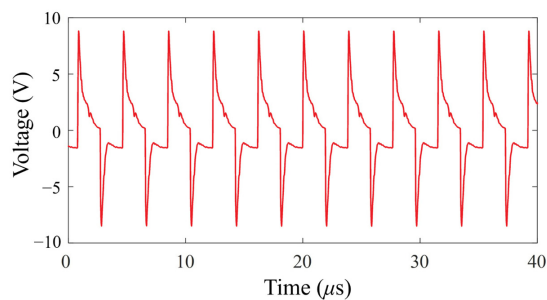


Figure 19. PV module diode-bypass failures.

First, the normal signal of a module in Figure 16 was observed. The output voltage waveform showed the peak voltage drop resulting from the component voltage drop in the PV module. There was no noticeable change in the negative half-cycle. The positive half-cycle had a micro fluctuation between 0 V and 5 V, and the variation can be used as a recognition signal. As the variation was insignificant, it was unlikely to be observed in the waveform, and the main features could be displayed using SDP. Afterward, the signal of a poor connection on a module was observed, as shown in Figure 17. In comparison to normal signals from a PV module, the peak-to-peak value of the voltage was a little lower than the characteristic of normal signals. As shown in Figure 18, when observing the module breakage signals, apparent fluctuations were observed between -10 V and 5 V in comparison to the normal signals of a PV module. Finally, the diode bypass failure signal was observed, as shown in Figure 19. The output waveform was approximate to the normal signal of a PV module. The voltage difference required observation for an extended period.

The data were extracted by the data processing unit and imported into the SDP. Four snowflake feature maps of different states can be drawn, as shown in Figures 20–23. The CNN used them for image recognition to diagnose the PV module fault type.

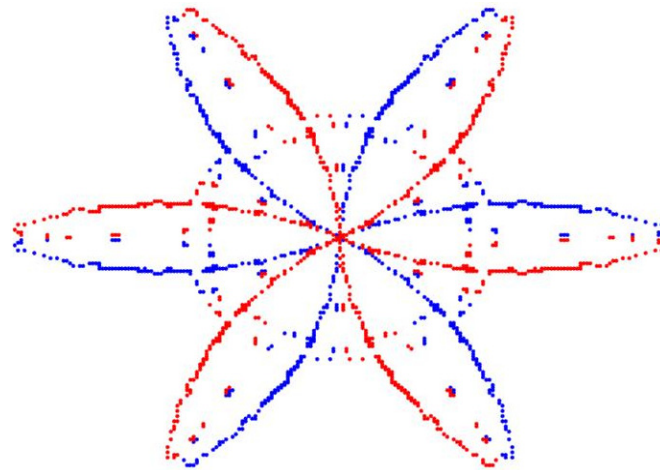


Figure 20. A normal PV module.

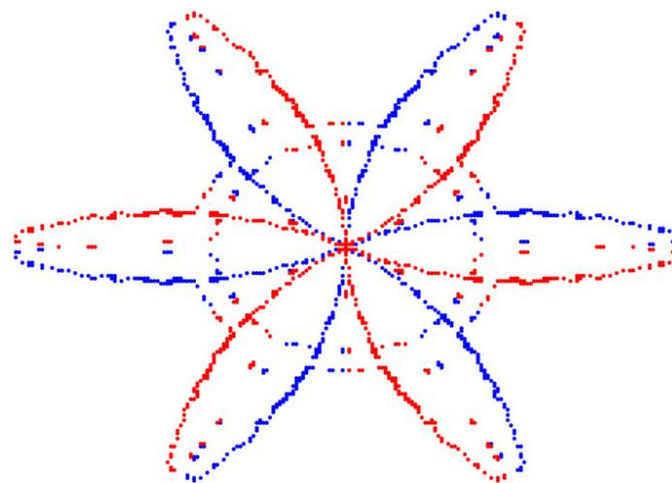


Figure 21. A poor connection on a PV module.

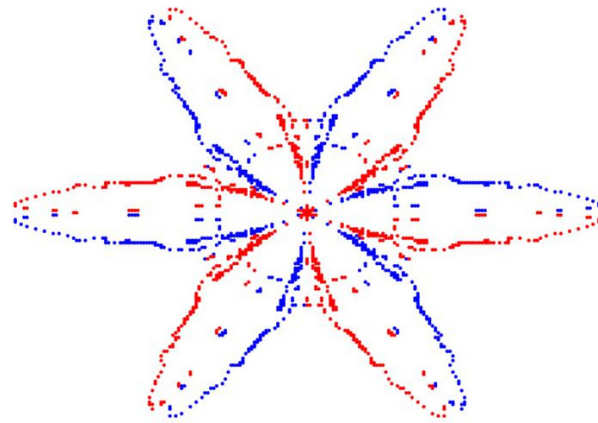


Figure 22. A PV module breakage.

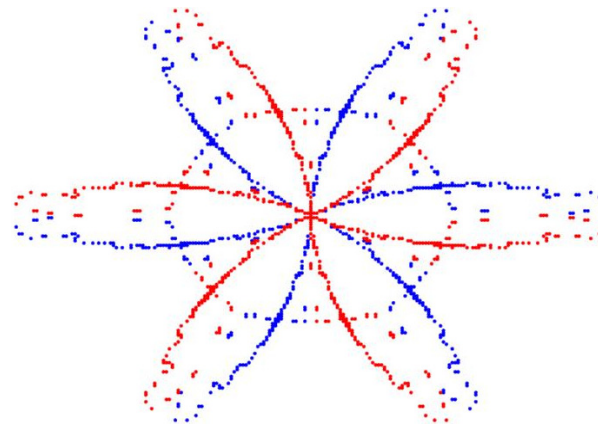


Figure 23. A PV module diode bypass failure.

Recognition Result

The CNN recognition model used in this study comprised three convolution layers, three pooling layers, and one fully connected layer. The model used a convolution kernel of 3×3 and ReLU as an activation function. The filter of the pooling layer of max pooling is shown in Figure 24.

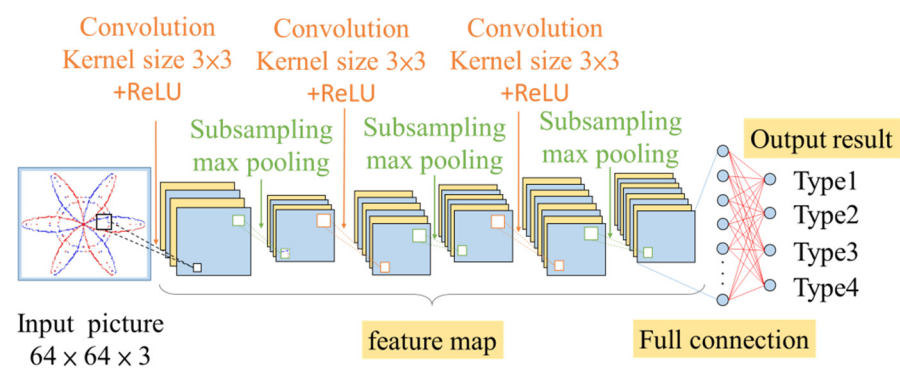


Figure 24. CNN model architecture.

The simulation results are shown in Table 3, with the SDP + CNN having the highest recognition accuracy of 99.88% and the accuracy of SDP + HOG + ENN being 91.75%. The training learning accuracy of CNN was 100%, and that of ENN was only 96.31%. In terms of training and recognition time, the SDP + HOG + ENN needs 3518 s, which is

very time-consuming for training, with an accuracy of 100% and 1.63 s for recognition. In contrast, the proposed method (SDP + CNN) only needs 181 s for training with an accuracy of 96.31% and 0.24 s for recognition.

Table 3. Comparison of CNN and ENN recognition results.

| Algorithm | Training Time (s) | Testing Time (s) | Epoch | Training Rate (%) | Accuracy Rate (%) | Ranking |
|-----------------|-------------------|------------------|-------|-------------------|-------------------|---------|
| SDP + CNN | 181 | 0.24 | 100 | 100 | 99.88 | 1 |
| SDP + HOG + ENN | 3518 | 1.63 | 100 | 96.31 | 91.75 | 2 |

Additionally, the recognition result of the PV modules was displayed in the confusion matrix, as shown in Figure 25. The x-axis is the actual fault type, and the y-axis is the predicted fault type. The green and red grids in the confusion matrix represent the number of accurate recognitions and the number of misrecognitions, respectively. The recognition accuracy and misrecognition rate of the specific fault types are the green and red values in the x-axis light gray grids. The overall recognition accuracy and misrecognition rate are the green and red values in the lower rightmost dark gray grids of the confusion matrix. The overall recognition accuracy is the total value of green grids divided by the total value of green and red grids. Taking Type 2 in Figure 25 as an example, the proposed method correctly identified 199 of 200 test data records with a recognition accuracy of 99.5%. Similarly, the Type 1, Type 3, and Type 4 recognition was 100%. Finally, the total value of the green grids was divided by the total value of green and red grids to obtain the total recognition accuracy rate of 99.88%.

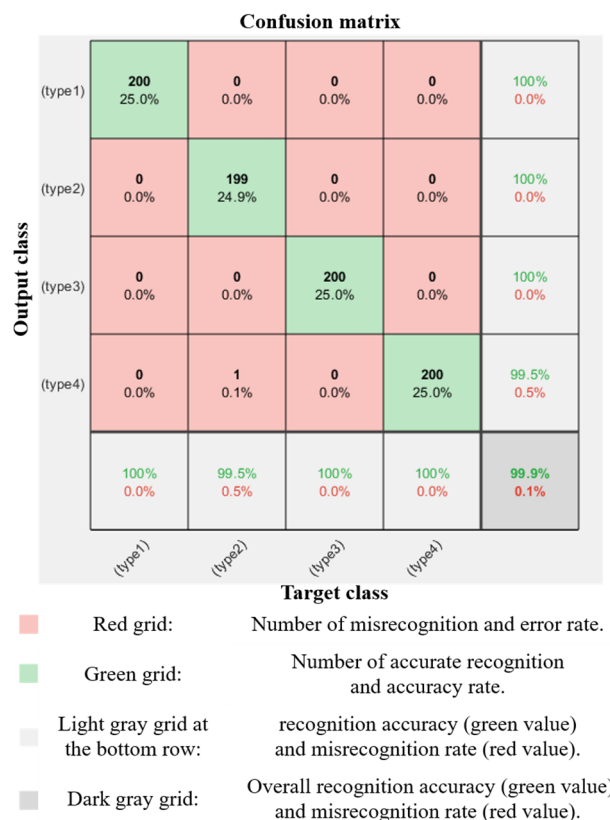


Figure 25. A confusion matrix of fault diagnosis.

5. Conclusions

This study successfully combined SDP with CNN to develop a PV module fault diagnosis system for the common fault types of PV modules. The snowflake image was used as a feature and combined with CNN for PV module state analyses. Based on the

actual measurements, the diagnosis algorithm proposed in this study is better than ENN and has a good diagnostic accuracy. Its recognition accuracy is 99.88%, proving that the proposed method is effective in the fault detection on PV modules. The proposed method captures the fault signals effectively, displays them in images, and accurately identifies the PV module fault type. The proposed method can be used in other domains concerning electricity and energy in the future, such as generators, power capacitors, and wind-power generation systems.

Author Contributions: M.-H.W. conceived the presented idea, and designed; S.-D.L. supervised the findings of this work, planned the experiments, and writing—review and editing; Z.-H.L. performed the numerical simulations, and writing—original draft preparation; all authors provided critical feedback and helped shape the research, analysis, and manuscript. All authors have read and agreed to the published version of the manuscript.

Funding: The authors gratefully acknowledge the financial support of the Ministry of Science and Technology of Taiwan, under contract number: MOST 110-2221-E-167-008-MY3.

Conflicts of Interest: The authors declare no conflict of interest.

Nomenclature

| | |
|-------------------|---|
| I_{SC} | Short circuit current |
| V_{mpp} | Voltage at maximum power point |
| ENN | Extension neural network |
| CSDM | Chaos synchronization detection method |
| V_{p-p} | Voltage peak to peak value |
| $r(i)$ | Radius of polar coordinates in the snowflake image |
| $\theta_{cw}(i)$ | Clockwise rotation angle of the x-axis |
| $\theta_{ccw}(i)$ | Counterclockwise rotation angle of the x-axis |
| x_i | i th sampling point of signal x |
| $x_{i+\tau}$ | Sampling point at No. $i + \tau$ time of signal x |
| x_{max} | Maximum value of the original signal |
| x_{min} | Minimum value of the original signal |
| τ | Signal interval time parameter |
| θ | Initial deflection angle of the x-axis |
| S | Amplification coefficient of rotation angle |
| x_j^l | No. j element of layer l |
| M_j | No. j convolution region of $l - 1$ layer feature image |
| W_{ij}^l | Weighting matrix corresponding to the convolution kernel |
| b_j^l | Deviation |
| $h(\cdot)$ | Output of a fully connected layer |
| X | Input of a fully connected layer |
| b | Additive deviation |
| $f(\cdot)$ | Activation function |

References

1. Tobias, R.R.; Mital, M.E.; Lauguico, S.; Guillermo, M.; Naidas, J.R.; Lopena, M.; Dizon, M.E.; Dadios, E. Design and Construction of a Solar Energy Module for Optimizing Solar Energy Efficiency. In Proceedings of the 2020 IEEE 12th International Conference on Humanoid, Nanotechnology, Information Technology, Communication and Control, Environment, and Management (HNICEM), Manila, Philippines, 3–7 December 2020.
2. Ayadi, F.; Colak, I.; Garip, I.; Bulbul, H.I. Targets of Countries in Renewable Energy. In Proceedings of the 2020 9th International Conference on Renewable Energy Research and Application (ICRERA), Glasgow, UK, 27–30 September 2020.
3. Ayadi, F.; Colak, I.; Garip, I.; Bulbul, H.I. Impacts of Renewable Energy Resources in Smart Grid. In Proceedings of the 2020 8th International Conference on Smart Grid (icSmartGrid), Paris, France, 17–19 June 2020.
4. Usova, M.A.; Velkin, V.I. Possibility to use renewable energy sources for increasing the reliability of the responsible energy consumers on the enterprise. In Proceedings of the 2018 17th International Ural Conference on AC Electric Drives (ACED), Ekaterinburg, Russia, 26–30 March 2018.

5. Matusz-Kalász, D.; Bodnár, I. Monitoring and Diagnostics of Photovoltaic Cells by Electroluminescence. In Proceedings of the 2022 23rd International Carpathian Control Conference (ICCC), Sinaia, Romania, 29 May–1 June 2022.
6. Lv, R.; Tang, J.; Jaubert, J.N.; Xing, G. Highly Accelerated Thermal Cycling Test for New Type of Crystalline Silicon Photovoltaic Modules. In Proceedings of the 2019 IEEE 46th Photovoltaic Specialists Conference (PVSC), Chicago, IL, USA, 16–21 June 2019.
7. Predan, F.; Franke, A.; Hoehn, O.; Lackner, D.; Helmers, H.; Siefer, G.; Bett, A.W.; Dimroth, F. Wafer-bonded GaInP/GaAs/GaInAs/GaSb four-junction solar cells with 43.8% efficiency under concentration. In Proceedings of the 2020 47th IEEE Photovoltaic Specialists Conference (PVSC), Calgary, AB, Canada, 15 June–21 August 2020.
8. Golive, Y.R.; Zachariah, S.; Bhaduri, S.; Dubey, R.; Chattopadhyay, S.; Singh, H.K.; Kottantharayil, A.; Shiradkar, N.; Vasi, J. Analysis and Failure Modes of Highly Degraded PV Modules Inspected during the 2018 All India Survey of PV Module Reliability. In Proceedings of the 2020 4th IEEE Electron Devices Technology & Manufacturing Conference (EDTM), Penang, Malaysia, 6–21 April 2020.
9. Mehmood, A.; Sher, H.A.; Murtaza, A.F.; Al-Haddad, K. Fault Detection, Classification and Localization Algorithm for Photovoltaic Array. *IEEE Trans. Energy Convers.* **2021**, *36*, 2945–2955. [[CrossRef](#)]
10. Mehmood, A.; Sher, H.A.; Murtaza, A.F.; Al-Haddad, K. A Diode-Based Fault Detection, Classification, and Localization Method for Photovoltaic Array. *IEEE Trans. Instrum. Meas.* **2021**, *70*, 3516812. [[CrossRef](#)]
11. Zhang, J.; Ai, C.; Zheng, Z.; Ding, K.; Chen, X.; Liu, Y.; Chen, L. Module-Level Fault Diagnosis of Photovoltaic Array based on Wireless Sensor Networks and Inverter Activated I-V Scanning. In Proceedings of the 2022 IEEE 5th International Electrical and Energy Conference (CIEEC), Nangjing, China, 27–29 May 2022.
12. Cai, X.; Wai, R.J. Intelligent DC Arc-Fault Detection of Solar PV Power Generation System via Optimized VMD-Based Signal Processing and PSO-SVM Classifier. *IEEE J. Photovolt.* **2022**, *12*, 1058–1077. [[CrossRef](#)]
13. Dhimish, M.; Chen, Z. Novel Open-Circuit Photovoltaic Bypass Diode Fault Detection Algorithm. *IEEE J. Photovolt.* **2019**, *9*, 1819–1827. [[CrossRef](#)]
14. Serfa Juan, R.O.; Kim, J. Photovoltaic Cell Defect Detection Model based-on Extracted Electroluminescence Images using SVM Classifier. In Proceedings of the 2020 International Conference on Artificial Intelligence in Information and Communication (ICAIIIC), Fukuoka, Japan, 19–21 February 2020.
15. Yun, L.; Bofeng, Y.; Dan, Q.; Fengshuo, L. Research on Fault Diagnosis of Photovoltaic Array Based on Random Forest Algorithm. In Proceedings of the 2021 IEEE International Conference on Power Electronics, Computer Applications (ICPECA), Shenyang, China, 22–24 January 2021.
16. Lu, S.D.; Wei, S.E.; Wang, M.H.; Sian, H.-W.; Kuo, C.-C. Hybrid Methodology Based on Extension Neural Network for Fault Diagnosis of Photovoltaic Module. *Sens. Mater.* **2021**, *33*, 2925–2941. [[CrossRef](#)]
17. Lu, S.-D.; Wang, M.-H.; Wei, S.-E.; Liu, H.-D.; Wu, C.-C. Photovoltaic Module Fault Detection Based on a Convolutional Neural Network. *Processes* **2021**, *9*, 1635. [[CrossRef](#)]
18. Sizkouhi, A.M.; Aghaei, M.; Esmailifar, S.M. A deep convolutional encoder-decoder architecture for autonomous fault detection of PV plants using multi-copters. *Sol. Energy* **2021**, *223*, 217–228. [[CrossRef](#)]
19. Trinh, N.T.N.; Hung, D.T.; Dat, N.H.T.; Dung, P.Q. Application of Artificial Intelligence in Detecting and Classifying Faults of Solar Panels. In Proceedings of the 2022 IEEE Ninth International Conference on Communications and Electronics (ICCE), Nha Trang, Vietnam, 27–29 July 2022.
20. Al-Katheri, A.A.; Al-Ammar, E.A.; Alotaibi, M.; Ghazi, G.A. Artificial Neural Network Application for Faults Detection in PV Systems. In Proceedings of the 2022 IEEE Delhi Section Conference (DELCON), New Delhi, India, 11–13 February 2022.
21. Lu, H.; Zhao, X.; Tao, B.; Yin, Z. Online Process Monitoring Based on Vibration-Surface Quality Map for Robotic Grinding. *IEEE/ASME Trans. Mechatron.* **2020**, *25*, 2882–2892. [[CrossRef](#)]
22. Yang, J.; Yan, R. A Multidimensional Feature Extraction and Selection Method for ECG Arrhythmias Classification. *IEEE Sens. J.* **2020**, *21*, 14180–14190. [[CrossRef](#)]
23. Zhu, X.; Zhao, J.; Hou, D.; Han, Z. An SDP Characteristic Information Fusion-Based CNN Vibration Fault Diagnosis Method. *Hindawi Shock Vibration Vol.* **2019**, *2019*, 3926963. [[CrossRef](#)]
24. Shrestha, S.M.; Mallineni, J.K.; Yedidi, K.R.; Knisely, B.; Tatapudi, S.; Kuitche, J.; Tamizhmani, G. Determination of Dominant Failure Modes Using FMECA on the Field Deployed c-Si Modules Under Hot-Dry Desert Climate. *IEEE J. Photovolt.* **2014**, *5*, 174–182. [[CrossRef](#)]
25. Tatapudi, S.; Libby, C.; Raupp, C.; Srinivasan, D.; Kuitche, J.; Bicer, B.; Tamizhmani, G. Defect and safety inspection of 6 PV technologies from 56,000 modules representing 257,000 modules in 4 climatic regions of the United States. In Proceedings of the 2016 IEEE 43rd Photovoltaic Specialists Conference (PVSC), Portland, OR, USA, 5–10 June 2016.
26. Brooks, A.E.; Cormode, D.; Cronin, A.D.; Kam-Lum, E. PV system power loss and module damage due to partial shade and bypass diode failure depend on cell behavior in reverse bias. In Proceedings of the 2015 IEEE 42nd Photovoltaic Specialist Conference (PVSC), New Orleans, LA, USA, 14–19 June 2015.
27. Yeh, C.W.; Chen, R. Using Convolutional Neural Network for Vibration Fault Diagnosis Monitoring in Machinery. In Proceedings of the 2018 IEEE International Conference on Advanced Manufacturing (ICAM), Yunlin, Taiwan, 16–18 November 2018.

28. Aziz, F.; Haq, A.U.; Ahmad, S.; Mahmoud, Y.; Jalal, M.; Ali, U. A Novel Convolutional Neural Network-Based Approach for Fault Classification in Photovoltaic Arrays. *IEEE Access* **2020**, *8*, 41889–41904. [[CrossRef](#)]
29. Krizhevsky, A.; Sutskever, I.; Hinton, G.E. ImageNet Classification with Deep Convolutional Neural Networks. *Assoc. Comput. Mach.* **2017**, *60*, 84–90. [[CrossRef](#)]
30. Wang, H.; Xu, J.; Yan, R. Bearing Fault Diagnosis Based on Visual Symmetrized Dot Pattern and CNNs. In Proceedings of the 2019 IEEE International Instrumentation and Measurement Technology Conference (I2MTC), Auckland, New Zealand, 20–23 May 2019.